Doppler spectrum of radio wave

scattering from ocean-like moving surfaces

for a finite illuminated area

Yukiharu Hisaki

Physical Oceanography Laboratory

Department of Physics and Earth Sciences

Faculty of Science

University of the Ryukyus

Short title: Doppler spectrum from moving waves

Abstract

It is necessary to understand how the Doppler peak frequency in the Doppler spectrum of radio wave scattering from moving waves is determined for practical applications such as oceanographic remote sensing. The author investigated Doppler peak frequency by using the integral equation method (IEM) for V-V polarization and a one-dimensional surface and by calculating the Doppler spectra of backscattered signals at moderate incidence for a finite illuminated area. In some cases, the Doppler peak frequency in Doppler spectra are determined from the surface wave frequency and not from the phase velocity of the surface wave, if the illuminated area is finite. The author investigated scattering from a sinusoidal wave for various radar and wave parameters. Doppler peaks were revealed at wave frequencies and higher-order harmonics of the Doppler peaks appeared in most cases. However, Doppler peaks whose position was close to the wave phase velocity-Doppler frequency became dominant as the phase difference of the reflected radio wave within the illuminated area became smaller. The appearance of wave phase velocity-Doppler peaks was limited when quasi-coherent scattering dominated. This interpretation can be applied to Bragg scattering, for which the Bragg wave phase velocity-Doppler frequency is identically equal to the wave frequency of the Bragg wave.

1 Introduction

We need to understand scattering of radio waves from moving rough waves for practical applications such as oceanographic remote sensing. To compute radio scattering from conducting rough surfaces, the integral equation method (IEM) has widely been used by numerous investigators for more than two decades [e.g., Lentz, 1974].

However, most investigators have concentrated on a comparison of numerical solutions with approximate methods such as the small perturbation method (SPM) and Kirchoff approximation (KA) [e.g., Fung and Chen, 1985; Chen and Fung, 1988], or on improving numerical techniques to reduce computational time [e.g., Chen, 1996]. Most of them have treated non-moving surface. Investigators who have treated moving surfaces are quite scarce, and consequently our understanding of Doppler spectra is not satisfactory.

For example, to the author's knowledge, the answer to the fundamental question of how the Doppler peak frequency in the Doppler spectrum of radio wave scattering from moving waves for a finite illuminated area is determined has not been investigated. There are two possible solutions: The first is that the Doppler peak frequency is equal to the wave frequency, because the amplitude of scattered radio wave signals varies along with the phase of a wave acting as a scatterer. As a result, the amplitude varies with a period of the wave period and the power spectrum of scattered signals has a peaks at the wave frequency. In fact, the Doppler peak frequency in the Doppler spectrum of a scattered signal calculated by the small perturbation method is equal to the wave frequency as shown in Appendix A (Eq. (A16)) and Hisaki and Tokuda [2001]. If we consider perturbation expansion to the higher-order, the Doppler peak frequency is expressed by the sum the wave frequencies (Hisaki and Tokuda [2001]).

The other possible answer is that Doppler peak frequency in the Doppler spectrum is determined by the Doppler shift corresponding to the wave phase velocity. It is widely believed that

the Doppler shift is determined from the line-of-sight velocity of the scatterer and the latter one is correct. However, as shown later from mathematics (Appendix A (Eq. (A16)) and Hisaki and Tokuda [2001]) and numerical computations (e.g., Figure 7a), the Doppler peak frequency is determined from the surface wave frequency and not from the phase velocity of the surface wave in some cases, if the illuminated area is finite.

Bragg scattering dominates in the case of radio wave scattering from randomly rough surface waves. The Doppler frequency by Bragg scattering (Bragg frequency) is the same as both the frequency of the wave contributing to Bragg scattering (Bragg wave) and Doppler shift derived from the phase velocity of the Bragg wave (Bragg wave phase velocity). Let ω_B be a frequency of the Bragg wave, k_i be a radio wave number, and θ_i be an incident angle. The Bragg wave number is $2k_i \sin \theta_i$, and the Bragg wave phase velocity is $v_B = \omega_B/(2k_i \sin \theta_i)$. Therefore, the Doppler frequency derived from the phase velocity $\omega_D = 2v_B \sin \theta_i \omega_0/c = \omega_B$, where ω_0 is a radio frequency and $c = \omega_0/k_i$ is the light velocity. That is, the wave frequency of the Bragg wave (ω_B) is identically equal to the Doppler frequency derived from the Bragg wave phase velocity (ω_D). Although this mathematical explanation to the fact that $\omega_D = \omega_B$ in the case of Bragg scattering is well known, there are few physical explanations to this fact. The few studies [Kwoh and Lake 1984; Thompson 1989; Rino et al. 1991] in which the time-varying properties of scattered signals based on IEM were calculated did not give the interpretation to the fact that $\omega_D = \omega_B$ in the case of Bragg scattering.

The subject of this study is to investigate the Doppler spectra of scattered radio waves from moving waves using IEM. The main objective is to identify the part of the wave motion which determines Doppler shift and/or Doppler spectrum of radio wave scattering from moving waves under different conditions of wave and radar parameters. The purpose of this study is not accurate prediction of Doppler spectra scattered from the sea. We must eliminate Bragg

3

scattering from our problem because it is so much stronger than the scattering we want to consider. Therefore, idealized situations for surface waves as scatterers are considered.

After reviewing the formulation and description of the method of the computation in Sections 2, the author shows the Doppler spectra of radio wave scattering from moving sinusoidal waves and he investigates the radar and wave parameter dependencies of the Doppler peak frequency in Section 3. The scatterers considered here are moving waves like ocean waves but are not limited to real ocean waves. It should be noted that the IEM used here is rigorously correct only for non time-varying surfaces. However, since Doppler frequencies and surface wave frequencies are much smaller than the radio wave frequencies, it is possible to regard surfaces as to be "frozen" at each time and to use the IEM for non time-varying surfaces. A discussion and conclusions are presented in Section 4.

2   Formulation

Figure 1 shows the scattering geometry. The horizontal coordinates are (x, y), and the z is the vertical coordinate. The surface displacement $\eta = \eta(y) = \eta(y, t)$ is independent of x, where t is the time. The incident radio wave number is k_i, and the incident angle is θ_i.

To compute backscattered signals from a perfectly conducting surface and V-V polarization, we must solve the tangential component of the surface current $J_t(y, \eta(y))$, which is governed by the magnetic field integral equation (MFIE) as

$$H_{inc}(y, \eta(y)) = -\frac{1}{2} J_t(y, \eta(y)) + \frac{i}{4} k_i \int_{-D}^{D} \Big[J_t(y', \eta(y', t)) H_1^{(2)}(k_i r)$$
$$\cos(\Phi_{ns}) \Big] \Big[1 + (\frac{\partial \eta}{\partial y'})^2 \Big]^{\frac{1}{2}} dy'. \tag{1}$$

This is where $H_\nu^{(\tau)}(z)$ is the ν-th order Hankel function of the τ-th kind, $H_{inc}(y, z)$ is the incident magnetic field, $[-D, D]$ is the integrated area, and $r = [(y - y')^2 + (\eta(y) - \eta(y'))^2]^{\frac{1}{2}}$ is the distance

4

between observation point $(y, \eta(y))$ and source point $(y', \eta(y'))$. The angle $\Phi_{ns} = Arc\cos(\mathbf{n}_s \cdot \mathbf{r}_s)$ is the angle between surface normal vector $\mathbf{n}_s = (-\nabla\eta + \mathbf{e}_z)(|\nabla\eta|^2 + 1)^{-1/2}$ and unit vector $\mathbf{r}_s = (1/r)(y' - y, z' - z)$ directed from observation point (y, z) to source point (y', z'), where $\mathbf{e}_z$ is the unit vector along the z-axis. Strictly speaking, the IEM used here is correct only for non time-varying surfaces, because this IEM is derived for monochromatic radio waves. However, since Doppler frequencies and surface wave frequencies are much smaller than the radio wave frequencies, it is possible to regard surfaces as to be "frozen" at each time and to use the IEM for non time-varying surfaces

Equation (1) is converted to a matrix equation in the form

$$(-\frac{1}{2}\mathbf{I} + \mathbf{K})\mathbf{J} = \mathbf{h}, \tag{2}$$

where $\mathbf{I}$ is a unit matrix of $M \times M$ and M is the number of divisions of the segment $[-D, D]$. The element of the complex matrices $\mathbf{K}$, $\mathbf{J}$, and $\mathbf{h}$ are given in the following forms for

$$y = y_m = -D + \frac{2D}{M}(m + \frac{1}{2}) \quad (m = 0, .., M - 1) \tag{3}$$

as

$$K_{mn} = \frac{1}{4}k_i \int_{d_n}^{d_{n+1}} N_1(k_i r) \cos(\Phi_{ns}) \Big[1 + (\frac{\partial\eta}{\partial y'})^2\Big]^{\frac{1}{2}} dy'$$
$$+ \frac{i}{4}k_i \int_{d_n}^{d_{n+1}} J_1(k_i r) \cos(\Phi_{ns}) \Big[(\frac{\partial\eta}{\partial y'})^2 + 1\Big]^{\frac{1}{2}} dy',$$
$$(m, n = 0, .., M - 1) \tag{4}$$

$$J_n = J_t(y_n, \eta(y_n)) \qquad (n = 0, \ldots, M - 1), \tag{5}$$

and

$$h_m = H_{inc}(y_m, \eta(y_m)) \qquad (m = 0, \ldots, M - 1), \tag{6}$$

where

$$d_n = -D + \frac{2D}{M}n \qquad (n = 0, \ldots, M - 1), \tag{7}$$

and N_ν and J_ν are the ν-th order Neumann and Bessel functions, respectively. The real part of the diagnosis element for **K** has singularity, but it is calculated for $y = y_m$ as

$$Real(K_{mm}) = \frac{1}{\pi k_i} \frac{\partial^2 \eta(y)}{\partial y^2} \Big\{ \sum_{l=0}^{\infty} (a_l b_l) - \frac{1}{2}(k_i \epsilon)[1 + (\frac{\partial \eta(y)}{\partial y})^2]^{-1} \Big\}$$
$$+ \frac{1}{4} k_i \int_{d_n}^{d_{n+1}} D_1(k_i r) \cos(\Phi_{ns})[1 + (\frac{\partial \eta(y')}{\partial y'})^2]^{\frac{1}{2}} dy' \tag{8}$$

$$a_0 = \frac{1}{4}(k_i \epsilon)^3 [1 + (\frac{\partial \eta(y)}{\partial y})^2]^{\frac{1}{2}} \tag{9}$$

$$\frac{a_{l+1}}{a_l} = \frac{-1}{4(l+1)(l+2)}(k_i \epsilon)^2 [1 + (\frac{\partial \eta(y)}{\partial y})^2] \tag{10}$$

$$b_l = \frac{1}{2l+3} \Big[\log(k_i \epsilon) - \frac{1}{2l+3} + \frac{1}{2}\ln(1 + (\frac{\partial \eta(y)}{\partial y})^2) \Big], \tag{11}$$

$$D_\nu(z) = \frac{2}{\pi} J_\nu(z)(\gamma - \ln 2)$$
$$- \frac{1}{\pi}\Big(\frac{z}{2}\Big)^\nu \sum_{l=0}^{\infty} \frac{(-1)^l}{l!(\nu+l)!}\Big(\frac{z}{2}\Big)^{2l} \Big[\sum_{k=1}^{l}\frac{1}{k} + \sum_{k=1}^{\nu+l}\frac{1}{k}\Big] \tag{12}$$

$\gamma = 0.5772..$ is a Euler number and $\epsilon = D/M$.

The incident magnetic field is the plane wave written as

$$H_{inc} = G_T(y, z) \exp(-ik_i(y\sin\theta_i - z\cos\theta_i)), \tag{13}$$

and $G_T(y, z)$ is a taper function of the form

$$G_T(y, z) = \exp(-\frac{(y\cos\theta_i + z\sin\theta_i)^{2b}}{g_T^{2b}}), \tag{14}$$

where b is a parameter to express the beam pattern. The parameter g_T is expressed in terms of the effective illuminated area L_{eff}, which is defined as

$$L_{eff} = \int_{-\infty}^{\infty} [G_T(y, 0)]^2 dy, \tag{15}$$

or

$$g_T = 2^{\frac{1}{2n}-1}\Gamma(\frac{1}{2n} + 1)L_{eff}\cos\theta_i, \tag{16}$$

where Γ is the Gamma function.

The author calculated the far field magnetic field as

$$H_s = \frac{1}{2}\Big(\frac{k_i}{L_{eff}}\Big)^{\frac{1}{2}} \exp(-i(k_i R + \frac{3\pi}{4}))$$
$$\int_{-D}^{D}\Big[J_t(y', \eta(y')) \exp(-ik_i(\sin\theta_i y' - \cos\theta_i \eta(y')))\Big]$$
$$(\cos\theta_i + \sin\theta_i \frac{\partial\eta}{\partial y'})dy' \tag{17}$$

from estimated surface current $J_n = J_t(y_n, \eta(y_n))$ $(n = 0, .., M-1)$ by solving Eq. (2), where R is the distance between the observation point and the illuminated area.

The summary to calculate H_s are as follows: First, the surface current $\mathbf{J} = (J_n)$ is calculated from Eq. (2). The real parts of diagnosis elements for complex matrix $\mathbf{K}$ are calculated from Eqs. (3), (7), and (8)–(12). Other elements of complex matrix $\mathbf{K}$ are calculated from Eqs. (3), (7), and (4). The vector $\mathbf{h} = (h_m)$ is given by Eqs. (3), (6), (7), (13), (14), and (16). The matrix equation (2) is solved iteratively and the surface current $\mathbf{J} = (J_n)$ is estimated. Then, the far field magnetic field H_s is calculated from the surface current $\mathbf{J} = (J_n)$ by Eq. (17). A Doppler spectrum, which is a power spectrum of the scattered signal as a function of Doppler frequency $f_D = \omega_D/(2\pi)$, is obtained by calculating the power spectrum of complex time series $H_s = H_s(t) = H_s(j\Delta t)$ $(j = 0, \ldots, N_t - 1)$, where Δt is the time step and N_t is the total number of time series.

The surface displacement of a wave propagating to the negative y-direction is written as

$$\eta(y, t) = \sum_{j=0}^{N-1} A_{wj} \cos(\omega_{wj}t + k_{wj}y + \phi_{wj}), \tag{18}$$

where N is the number of wave components, A_{wj} is a wave amplitude, ω_{wj} is a wave angular frequency, k_{wj} is a wave number, ϕ_{wj} is a phase, and satisfying the linear dispersion relationship $\omega_{wj} = (gk_{wj})^{1/2}$, where g is the gravitational acceleration. Here, the effect of surface tension has been neglected for simplification.

3   Scattering from sinusoidal waves

3.1   Examples of numerical computations

The scattered signals from sinusoidal waves ($N = 1$ in Eq. (18) and $\phi_{w0} = 0$) were calculated. The parameters for the computation are in Table 1. To identify the part of wave motions contributing to Doppler frequencies, the rectangular beam form is preferred. Furthermore, the author calculated scattered signals for $b = 1$ in Eq. (14) (Gaussian beam form), and it is found that the integration range D must be very large since backscattered signals from sinusoidal waves are very weak. Therefore, it takes very long time to calculate scattered signals from sinusoidal waves by MFIE. Here, the parameter b in Eq. (14) is 10 (near-rectangular beam form), although it may be unrealistic and Doppler spectra may be affected by edge effects. In this example, the integration range D is much larger than the effective length L_{eff}, because the author computed scattered signal later for a large wave slope as the effect of shadowing may be significant. However, the constraint $2D/(M-1) < 2\pi/(5k_i)$ [Axline and Fung 1978] is satisfied in all of the computations presented here.

Figure 2 indicates the Doppler spectrum of scattered signal H_s for small wave amplitudes A_{w0}. For small wave amplitudes, the peaks of the Doppler spectrum appear almost at the wave frequency $\pm f_{w0}$. The scattered signal H_s varies significantly as the wave phase varies. As a result, the Doppler peaks can be seen at about $\pm f_{w0}$. The harmonics of the Doppler peaks become significant as the wave amplitude increases.

Figure 3 indicates the Doppler spectrum of scattered signal H_s for large wave amplitudes A_{w0}. In these examples, the time step Δt is 0.01 s. The other parameters are the same as those in Table 1.

A Doppler peak can be seen for $A_{w0} = 1$ m, whose position is different from the Doppler peak

corresponding to the wave phase velocity of the wave (wave phase velocity-Doppler frequency). This peak is close to the the wave phase velocity-Doppler frequency. as wave amplitudes larger, although the peak frequency is somewhat smaller than the the wave phase velocity-Doppler frequency. In Figure 2, the peak Doppler frequency of radio wave scattering from moving waves is determined by the wave frequency and not by the wave phase velocity for small wave amplitudes. In Figure 3, the peak Doppler frequency becomes closer to the wave phase velocity-Doppler frequency as larger wave amplitudes. Figure 3 are somewhat noisy, however, the author believes that the main features discussed here are valid.

3.2 Parameter dependency of the Doppler peak position

Although a Doppler peak corresponding to the wave phase velocity appears from $A_{w0} = 2.5$ m in the example presented here, the wave amplitude is too large. In fact, the amplitude A_{w0} must satisfy the constraint:

$$\frac{2A_{w0}}{\lambda_{w0}} \leq \frac{1}{7}, \tag{19}$$

although wave breaking is occurred at the wave slope lower than Eq. (19) in practice. Here, the author investigated the radio frequency dependence of Doppler spectra at the wave amplitude $A_{w0} = (1/20)\lambda_{w0} = 1$ m. To calculate the time series of scattered signal H_s, it takes long time to solve the MFIE, or Eq. (2), because the number of divisions in range M had to be large enough to resolve the radio wavelength. Therefore, since the effect of shadowing may not be significant at the wave slope and incident angle ($\theta_i = 45°$), the Kirchoff approximation (KA), in which the surface current $\mathbf{J}$ is approximated as

$$J_n = J_t(y_n, \eta(y_n)) \simeq -2H_{inc}(y_n, \eta(y_n)), \qquad (n = 0, \ldots, M-1) \tag{20}$$

(instead of estimating $\mathbf{J}$ by solving Eq. (2)), was used to compute scattered signal H_s.

To check the validity of computation, the Doppler spectra of scattered fields calculated by Kirchoff approximation and by MFIE were compared at the limiting wave amplitude $A_{w0} = (1/20)\lambda_{w0} = 1$ m. In this computation, $D = 2$ m, $\Delta t = 0.01$ s, and $M = 250$ while the other parameters were the same as those in Table 1.

Figure 4 compares the Doppler spectra, which agree well. Furthermore, the difference between Figure 4 and Figure 3a is small. Using Kirchoff approximation to calculate the Doppler spectra for the parameter as the wave amplitude $A_{w0} = 1$ m, incident angle $\theta_i \leq 45°$ and radio frequency $f_0 \geq 1$ GHz does not significantly alter the configuration for the Doppler spectra.

Figure 5 shows the radio frequency dependence of Doppler spectra for $A_{w0} = (1/20)\lambda_{w0} = 1$ m. In this computation, $D = 2$ m, $M = 2000$, $N_t = 8192$, $\Delta t = 0.001$ s and the Doppler frequencies corresponding to the wave phase velocity (f_{pD}) are respectively 26 Hz, 53 Hz, 132 Hz, 264 Hz, for radio frequency $f_0 = 1$ GHz, 2 GHz, 5 GHz and 10 GHz. The other parameters are the same as those in Table 1. The positions of the Doppler peaks are different from those of wave phase velocity-Doppler peaks this example even for the highest radio frequency.

To verify the calculation in Figure 5 that Doppler peaks whose position are close to wave phase velocity-Doppler peaks do not appear, the Doppler spectra were computed for $\theta_i = 15°$. The parameters in this computation were the same as those in Figure 5 except for incidence angle θ_i. Doppler frequencies corresponding to the wave phase velocity (f_{pD}) were respectively 9.6 Hz, 19.3 Hz, 48.2 Hz and 96.5 Hz, for radio frequencies $f_0 = 1$ GHz, 2 GHz, 5 GHz and 10 GHz.

Figure 6 shows the results. Doppler peaks corresponding to the wave phase velocity appear in these examples. Furthermore, the bandwidths of Doppler spectra in Figure 6 are larger than those in Figure 5, because the line-of-sight components of vertical motions of surface waves for $\theta_i = 15°$ are larger those for $\theta_i = 45°$. Figure 6 are somewhat affected by edge effects, however,

the author believes that the main features discussed here are valid.

In general, as the wave slope becomes larger or the incident angle becomes smaller, the quasi-coherent scattering dominates. Therefore, we can understand the appearance of Doppler peaks corresponding to wave phase velocity for larger wave amplitudes in Figure 3 and smaller incident angles in Figure 6.

To investigate the wave amplitude dependence of Doppler spectra for a fixed wave slope, Doppler spectra for various wave amplitudes $A_{w0} = (1/20)\lambda_{w0}$ m and $\theta_i = 15°$ were estimated from Kirchoff approximation.

In this estimation, $f_0 = 1$ GHz, $M = 2000$, $N_t = 8192$, $\Delta t = 0.005$ s and the Doppler frequencies corresponding to the wave phase velocity (f_{pD}) are respectively 0.965 Hz, 3.05 Hz, 9.65 Hz, and 30.5 Hz for wave amplitudes A_{w0} =0.01, 0.1, 1 and 10 m. These wavelenghts vary from 0.2 m to 200 m. The wave frequencies (f_{w0}) are respectively 2.79 Hz, 0.88 Hz, 0.28 Hz, and 0.088 Hz for wave amplitudes A_{w0} =0.01, 0.1, 1 and 10 m.

In these examples, the Doppler peak whose position is close to the wave phase velocity-Doppler frequency is seen for larger wave amplitudes (Figure 7c,d: $A_{w0} = 1, 10$ m). On the other hand, the Doppler peak corresponding to the wave frequency is prominent in Figure 7a ($A_{w0} = 0.01$ m, $f_{w0} = 2.79$ Hz). For the second smallest amplitude (Fig. 7 b: $A_{w0} = 0.1$ m, $f_{w0} = 0.88$ Hz), higher-order harmonics of the wave frequency are prominent and the harmonic close to the wave phase velocity-Doppler frequency (f_{pD}) is the largest in this example.

Furthermore, the author investigated the Doppler peak dependence of effective lengths for the illuminated area L_{eff}. Doppler spectra were computed using Kirchoff approximation for $L_{eff} = 0.1, 0.3, 1$ and 5 m. In this computation, $D = 20$, $M = 15000$, $N_t = 8192$, $\Delta t = 0.005$ s, $\theta_i = 15°$, $\lambda_{w0} = 1$ m, $A_{w0} = (1/20)\lambda_{w0} = 0.05$ m and $f_0 = 10$ GHz. Figure 8 shows the result. The wave phase velocity-Doppler peaks are seen in all examples. For larger illuminated area,

11

scattered signals varying along with the phase of a wave acting as a scatterer vanish. As a result, the wave phase velocity-Doppler peak is the most prominent in the largest illuminated area (Figure 8 d).

4   Discussion and Conclusions

The author investigated the scattering properties from sinusoidal waves for a finite illuminated area to answer the question: how is the Doppler peak frequency in the Doppler spectrum determined for scattering from moving waves ? This problem does not seem to be considered. The wave frequency of the Bragg wave is equal to the Doppler frequency derived from the Bragg wave phase velocity, i.e., $\omega_D = \omega_B$ in the case of Bragg scattering. Furthermore, it is believed that the Doppler shift is determined from the line-of-sight velocity of the scatteres, and the Doppler shift for scattering from surface waves is determined from the line-of-sight phase velocity of surface waves. However, as explained physically (Section 1), mathematically (Eq. (A16)) and numerically (e.g., Figure 7a), the Doppler peak frequency in the Doppler spectrum is determined from surface wave frequencies in some cases, if the illuminated area is finite.

To explain interpretation of the fact that the Doppler peak frequency is determined from the wave frequency, we write transmitted radio wave signals as $s(t) = \exp(-i\omega_0 t)$. Because amplitudes of scattered radio wave signals vary along with the phase of a wave acting as a scatterer, amplitudes of the scattered radio wave are written as $a(t) = \exp(-i\omega_w t)$, where ω_w is a radian frequency of a wave acting as a scatterer. Therefore, scattered signals are written as $p(t) = a(t)s(t) = \exp(-i(\omega_0 + \omega_w)t)$, which shows that Doppler frequency is equal to the wave frequency.

The author attempted to calculate scattered signals from sinusoidal waves based on MFIE or

12

KA. Although the MFIE is is rigorously correct only for monochromatic radio waves, we can regard surfaces as to be "frozen" at each time in this case and the MFIE is used. The author considered two kinds of incident beam patterns: Gaussian beam pattern ($b = 1$ in Eq. (14)) and near-rectangular beam pattern ($b = 10$ in Eq. (14)).

However, because backscattered signals from sinusoidal waves are very weak, it is not feasible to calculate scattered signals for $b = 1$. Therefore, the results only for $b = 10$ are presented for scattering from sinusoidal waves.

From numerical computations of Doppler spectra for various parameters, the Doppler peaks are at the wave frequency and harmonics of the Doppler peak appear in many cases. Furthermore, it was found that Doppler peaks whose position is close to the wave velocity-Doppler frequency became dominant (1) as the wave slope increased, (2) as the incident angle decreased, (3) as the wave amplitude increased and (4) as the illuminated area increased.

There is a tendency for the wave phase velocity-Doppler peaks to become prominent, where the wave slope parameter $2\pi A_{w0}/\lambda_{w0}$ is close to $\tan\theta_i$. Therefore, we can interpret the appearance of the Doppler peak as the dominance of the "quasi-coherent scattering." Here, the phase difference of the reflected radio wave is small within the illuminated area. Based on this interpretation, we can understand findings (1), (2) and (3) above as conditions for the appearance of the wave phase velocity-Doppler peak. It may appear that the finding (4) contradicts with other findings, however, this is not the case. As the illuminated area increases, the components in the scattered signals which vary along the phase of the surface wave significantly vanish, because the phase difference of these components is large within the illuminated area. As a result, the phase of the scattered radio waves contributing to the reception by the antenna is almost uniform, and we can interpret scattering in Figure 8d as quasi-coherent scattering.

It is possible to explain the fact that the Bragg frequency is identically equal to both the

Doppler shift derived from the phase velocity of the Bragg wave and the wave frequency of the Bragg wave in the same manner. As explained in Section 1 and Appendix A (Eq. (A16)), the Doppler frequency is equal to the frequency of the wave acting as a scatterer. On the other hand, in the case of Bragg scattering, that is, in the case that the illuminated length is large, the phase of the scattered radio waves contributing to the reception by the antenna is uniform. Therefore, the Doppler frequency by the Bragg wave is also equal to the Doppler shift corresponding to the phase velocity of the Bragg wave.

It should be noted that it is impossible to verify the results in Section 3 by the radar observation of the sea due to the overshadow by Bragg scattering. Even by the investigation of scattering from mechanically generated waves in the laboratory wave-tank experiment, the verification may be difficult. If anyone would like to verify these results, it may be necessary to investigate the scattering from "artificial conducting surfaces." Furthermore, we should investigate radio wave scattering for the ocean remote sensing using IEM and a sophisticated surface wave model.

Acknowlegement

Appendix A: Extension of first-order theory to finite illuminated area

Here, the author derives a small perturbation method for a finite illuminated area using the standard procedure by Rice [1951]. The magnetic field $\mathbf{H} = (H, 0, 0)$ is expressed using the

Rayleigh hypothesis as

$$H = H_A + 2G_T(y, 0) \exp(i(\omega_0 t - k_i \sin \theta_i y)) \cos(k_i \cos \theta_i z), \tag{A1}$$

where H_A is the scattered magnetic field written as

$$H_A = \int_{\mathbf{K}} dA(\mathbf{K}) \exp(i(\omega t - ky - \kappa(k)z)), \tag{A2}$$

$$\mathbf{K} = (\omega, k) \quad \kappa(k) = (k_i^2 - k^2)^{1/2} \tag{A3}$$

and k is the one-dimensional wave number vector, where dA is a random variable. The second term at the right of Eq. (A1) is the sum of incident and reflected field, and it does not contributes to scattering to the backscattering direction. We write surface displacement in Fourier-Stieltjes representation as

$$\eta(y, t) = \int_{\mathbf{K}} dN(\mathbf{K}) \exp(i(\omega t - ky)), \tag{A4}$$

where dN is a random variable. Using the the boundary condition $(\mathbf{n}_s \cdot \nabla)H = 0$ on the surface $z = \eta$, the random variable dA in Eq. (A2) is calculated by expanding the power series of η to the first order as

$$dA(\mathbf{K}) = G_T(y, 0)f_{A1}(k)dN(\mathbf{K} - \mathbf{K}_0), \tag{A5}$$

where

$$f_{A1}(k) = \frac{-2ik_i(k \sin \theta_i - k_i)}{\kappa(k)}, \tag{A6}$$

and where $\mathbf{K}_0 \equiv (\omega_0, k_0) = (\omega_0, k_i \sin \theta_i)$.

Then, we can calculate the far-field scattered field $H_s(t)$ using the tangential component of magnetic surface current $J_t = -H$ from Eq. (17) by expanding the power series of η. We can write the first order term as

$$H_s(t) = \frac{1}{2}\Big(\frac{k_i}{L_{eff}}\Big)^{\frac{1}{2}} \exp(-i(k_i R + \frac{3\pi}{4})) \int_{\mathbf{K}} dN(\mathbf{K} - \mathbf{K}_0)f_1(k) \exp(i\omega t), \tag{A7}$$

where

$$f_1(k) = \left[\int_{-D}^{D} \exp(-i(k+k_0)y')G_T(y',0)dy' \right] \left[\cos\theta_i f_{A1}(k) + 2i(k_i - k\sin\theta_i) \right] \tag{A8}$$

If we assume that dN is a Gaussian process with zero mean, by using the relation

$$\langle dN(\mathbf{K})dN(-\mathbf{K}_1) \rangle_E = X(\mathbf{K})\delta(\mathbf{K} - \mathbf{K}_1)d\mathbf{K}d\mathbf{K}_1, \tag{A9}$$

where $X(\mathbf{K})$ is a frequency-wave number ocean wave spectrum, and where $\langle \ldots \rangle_E$ denotes ensemble averaging, we can calculate the first-order radar cross section as

$$\sigma_1(\omega) = \frac{k_i}{4L_{eff}} \int_k |f_1(k)|^2 X(\mathbf{K} - \mathbf{K}_0)dk. \tag{A10}$$

We can simplify the radar cross section using

$$X(\mathbf{K}) = \frac{1}{2} \sum_{m=\pm 1} S(mk)\delta(\omega - m(g|k|)^{1/2}), \tag{A11}$$

$$S(mk)dk = \Psi_{(m)}(\omega)d\omega \qquad (m = \pm 1; \quad k = \frac{\omega^2}{g}) \tag{A12}$$

and

$$\Psi(\omega) = \Psi_{(-1)}(\omega) + \Psi_{(1)}(\omega) \tag{A13}$$

as

$$\sigma_1(\omega_D) = \frac{k_i}{8L_{eff}} \sum_{m=\pm 1} |f_1(-mk + k_0)|^2 \Psi_{(m)}(|\omega_D|) \quad (\text{for} \ \omega_D < 0, \ k = \frac{\omega_D^2}{g}) \tag{A14}$$

$$\sigma_1(\omega_D) = \frac{k_i}{8L_{eff}} \sum_{m=\pm 1} |f_1(mk + k_0)|^2 \Psi_{(m)}(|\omega_D|) \quad (\text{for} \ \omega_D > 0, \ k = \frac{\omega_D^2}{g}) \tag{A15}$$

where $S(k)$ is a wave number spectrum, and $\Psi_{(-1)}(\omega)$ and $\Psi_{(1)}(\omega)$ are wave frequency spectra composed of waves propagating to negative and positive directions, respectively. Thus, the following equation is derived:

$$\sigma(\omega_D) = F_c(-mk)\Psi(|\omega_D|) \tag{A16}$$

for waves propagating to the negative direction, where

$$F_c(k) = \frac{2k_i}{L_{eff}} \Big[\int_0^D \cos((k + 2k_i \sin\theta_i)y')G_T(y', 0)dy' \Big]^2$$
$$(k_i \cos^2\theta_i - k\sin\theta_i)^2 \Big| 1 + \frac{k_i \cos\theta_i}{\kappa(k_0 + k)} \Big|^2, \tag{A17}$$

and $k = \omega_D^2/g$. The sign m in Eq. (A16) is -1 for $\omega_D < 0$ and $m = 1$ for $\omega_D > 0$.

Equations (A14) and (A15) are reduced for $D \longrightarrow \infty$ and $L_{eff} \longrightarrow \infty$ as

$$\sigma_1(\omega_D) = 4\pi k_i^3(1 + \sin^2\theta_i)^2 S(-mk)\delta(\omega_D - m(2gk_0)^{1/2}), \tag{A18}$$

and Eq. (A18) is the radar cross section for Bragg scattering.

References

Axline R. M. and Fung A. K., 1978: Numerical computation of scattering from a perfectly conducting random surface, *IEEE Trans. Antennas Prop.,* **AP-26,** 482–487.

Chen F., 1996: The numerical calculation of two-dimensional rough surface scattering by conjugate gradient method. *Int. J. Remote Sensing,* **17,** 801–808.

Chen M. F. and A. K. Fung, 1988: A numerical study of the regions of validity of the Kirchoff and small-perturbation rough surface scattering models. *Radio Sci.,* **23,** 163–170.

Fung, A. K. and M. F. Chen, 1985: Numerical simulation of scattering from simple and composite random surfaces. *J. Opt. Soc. Am. A,* **2,** 2274–2284.

Hisaki, Y., and M. Tokuda, VHF and HF sea-echo Doppler spectrum for a finite illuminated

area. *Radio Sci.,* **3,** 425–440, 2001.

Kwoh, D. S. W. and B. M. Lake, 1984: A deterministic, coherent, and dual-polarized laboratory study of microwave backscattering from water waves, Part I: Short Gravity waves. *IEEE. J. Ocean. Eng.,* **OE-9,** 291–308.

Lentz, R. R., 1974: A numerical study of electromagnetic scattering from ocean-like surfaces. *Radio Sci.,* **9,** 1139–1146.

Rice, S. O., 1951: Reflection of electromagnetic waves from slightly rough surfaces. *Comm. Pure Appl. Math.,* **4,** 351–378.

Rino, C. L., L. C. Thomas, A. K. Koide, H. D. Ngo, and H. Guthart, 1991: Numerical simulation of backscatter from linear and nonlinear ocean surface realizations. *Radio Sci.,* **26,** 51–71.

Thompson, D. R., 1989: Calculation of microwave Doppler spectra from the ocean surface with a time-dependent composite model, in *Radar Scattering From Modulated Wind Waves,* edited by G. L. Komen and W. A. Oost, pp. 27–40, Kluwer Academic, Dordrecht, The Netherlands.

Table

$f_0 = \omega_0/(2\pi)$	radio frequency	1 GHz
θ_i	incidence angle	45°
$f_B = \omega_B/(2\pi)$	Bragg frequency	2.71 Hz
v_B	Bragg wave phase velocity	0.575 ms^{-1}
L_{eff}	effective length	1 m
D	integration range	10 m
N_t	total number of time series	512
M	number of divisions in the range	1000
Δt	time step to calculate scattered signal	0.05 s
$\lambda_{w0} = 2\pi/k_{w0}$	wavelength	20 m
$f_{w0} = \omega_{w0}/(2\pi)$	wave frequency	0.28 Hz
f_{pD}	Doppler frequency corresponding to the peak wave phase velocity	26.36 Hz

Table 1: Examples of parameters to calculate scattered signal.

Figures and captions
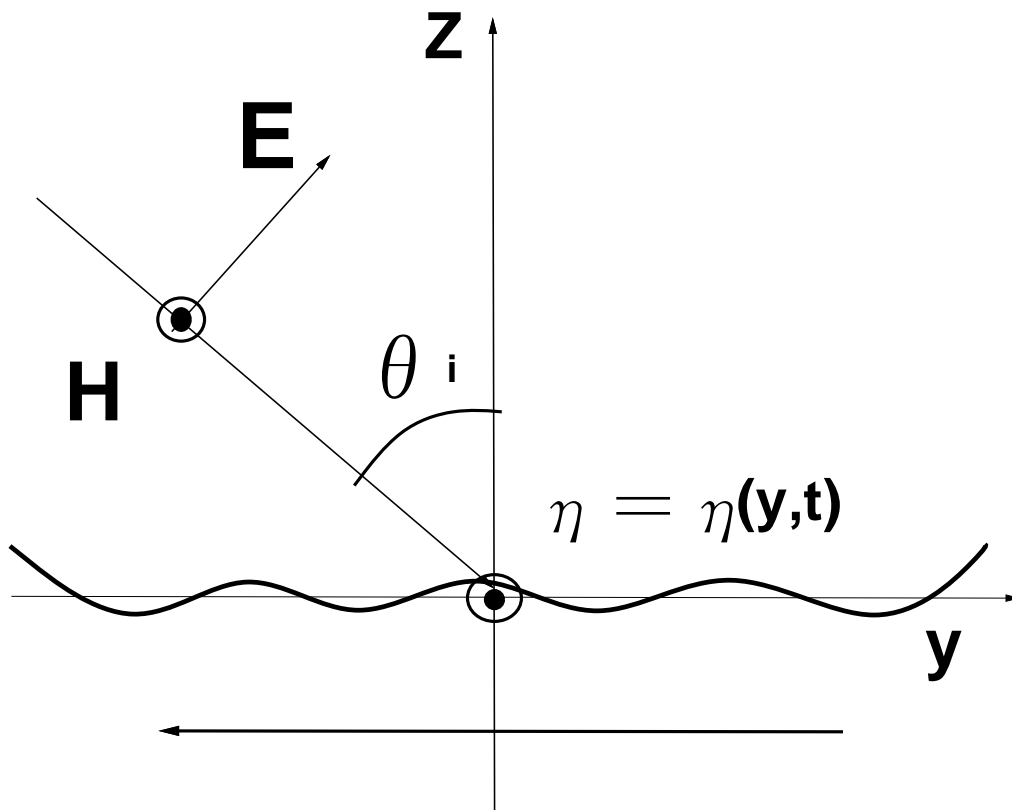
Figure 1: Scattering geometry.
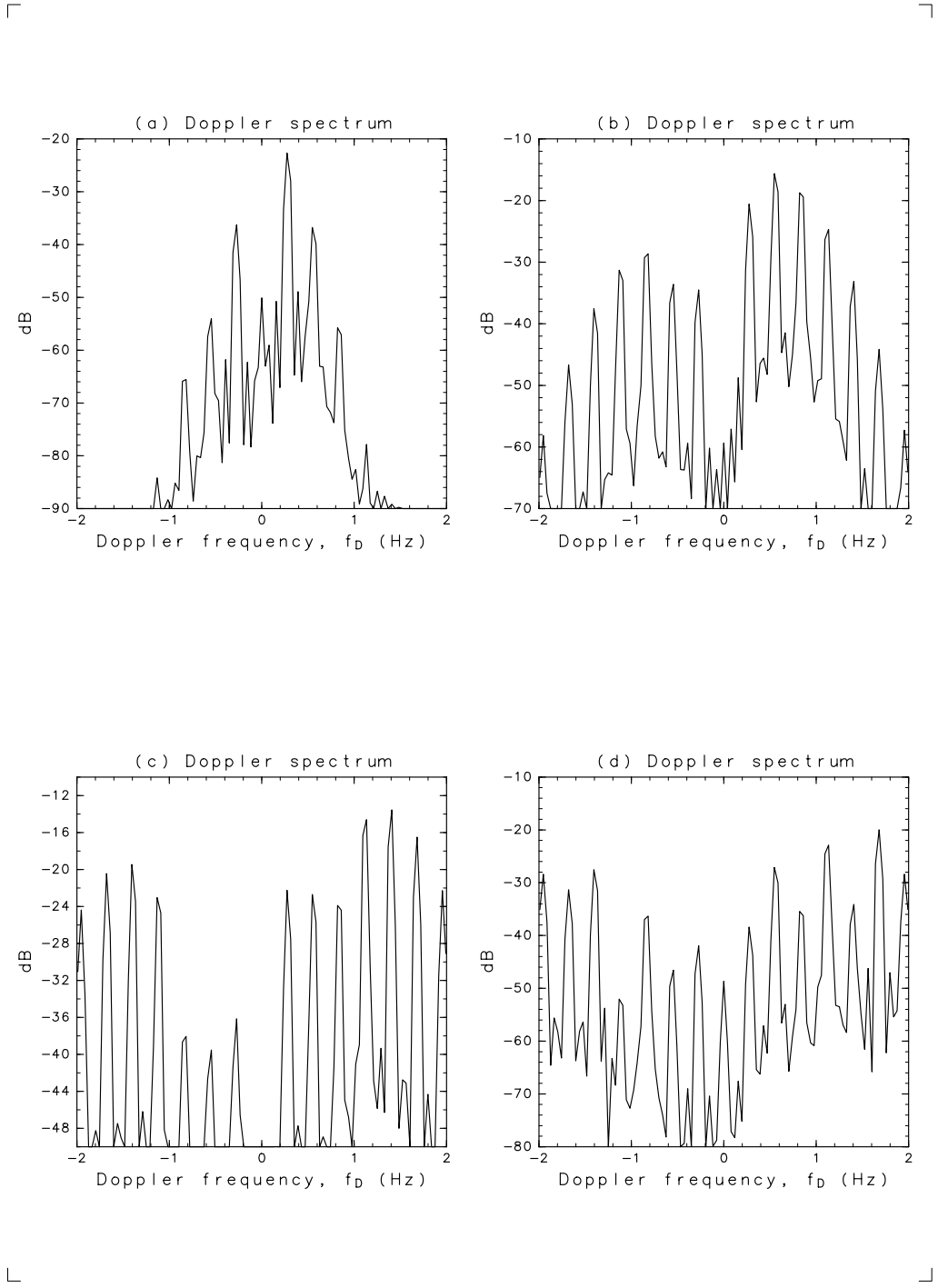
Figure 2: Doppler spectra estimated from MFIE for small wave amplitudes A_{w0}. (a) $A_{w0} = 0.01$ m, (b) $A_{w0} = 0.05$ m, (c) $A_{w0} = 0.1$ m, (d) $A_{w0} = 0.5$ m.
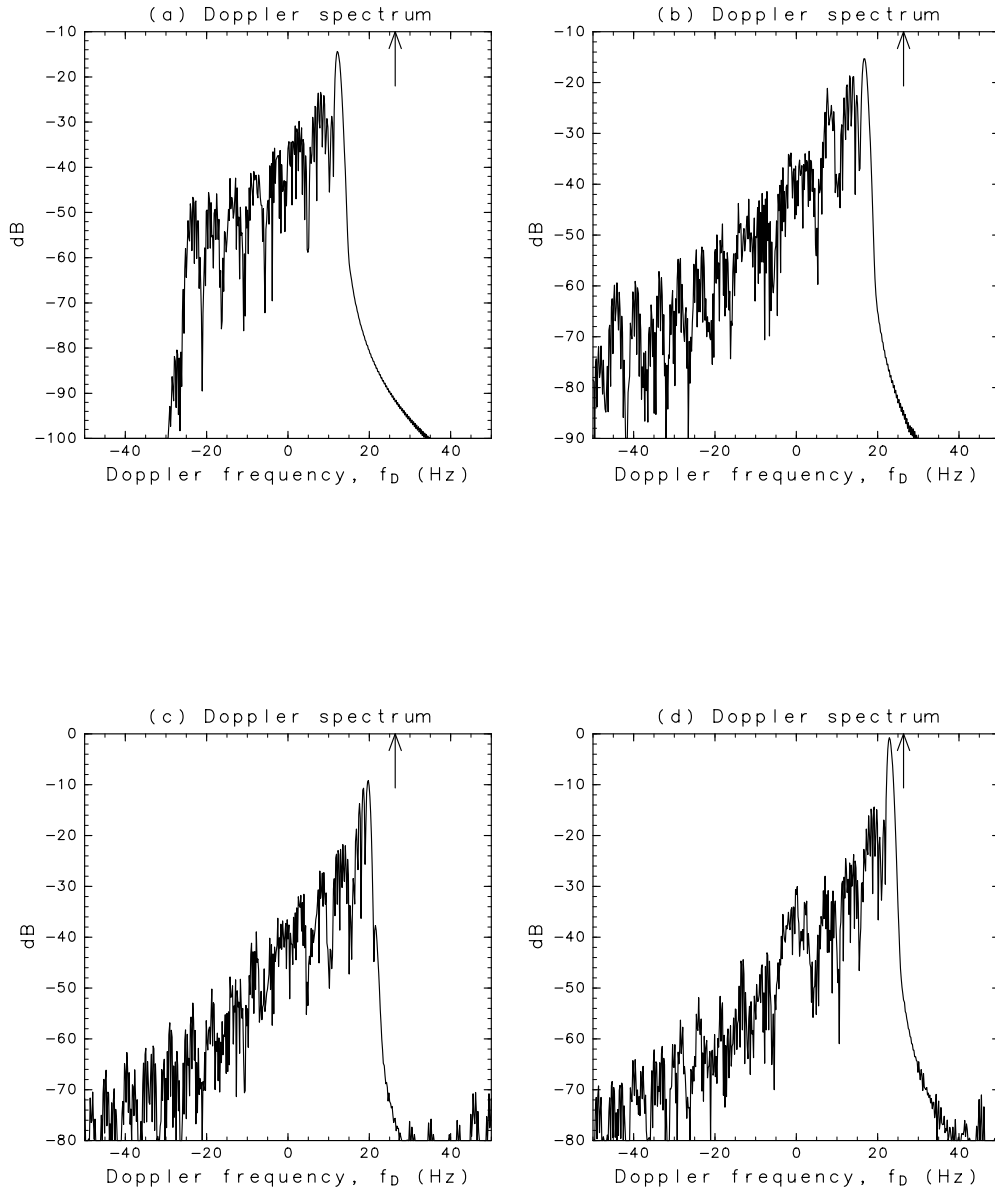
Figure 3: Doppler spectra estimated from MFIE for large wave amplitudes A_{w0}. The arrows on the upper horizontal axis indicate the position of the wave velocity-Doppler frequency. (a) $A_{w0} = 1.0$ m, (b) $A_{w0} = 1.5$ m, (c) $A_{w0} = 2.0$ m, (d) $A_{w0} = 2.5$ m.
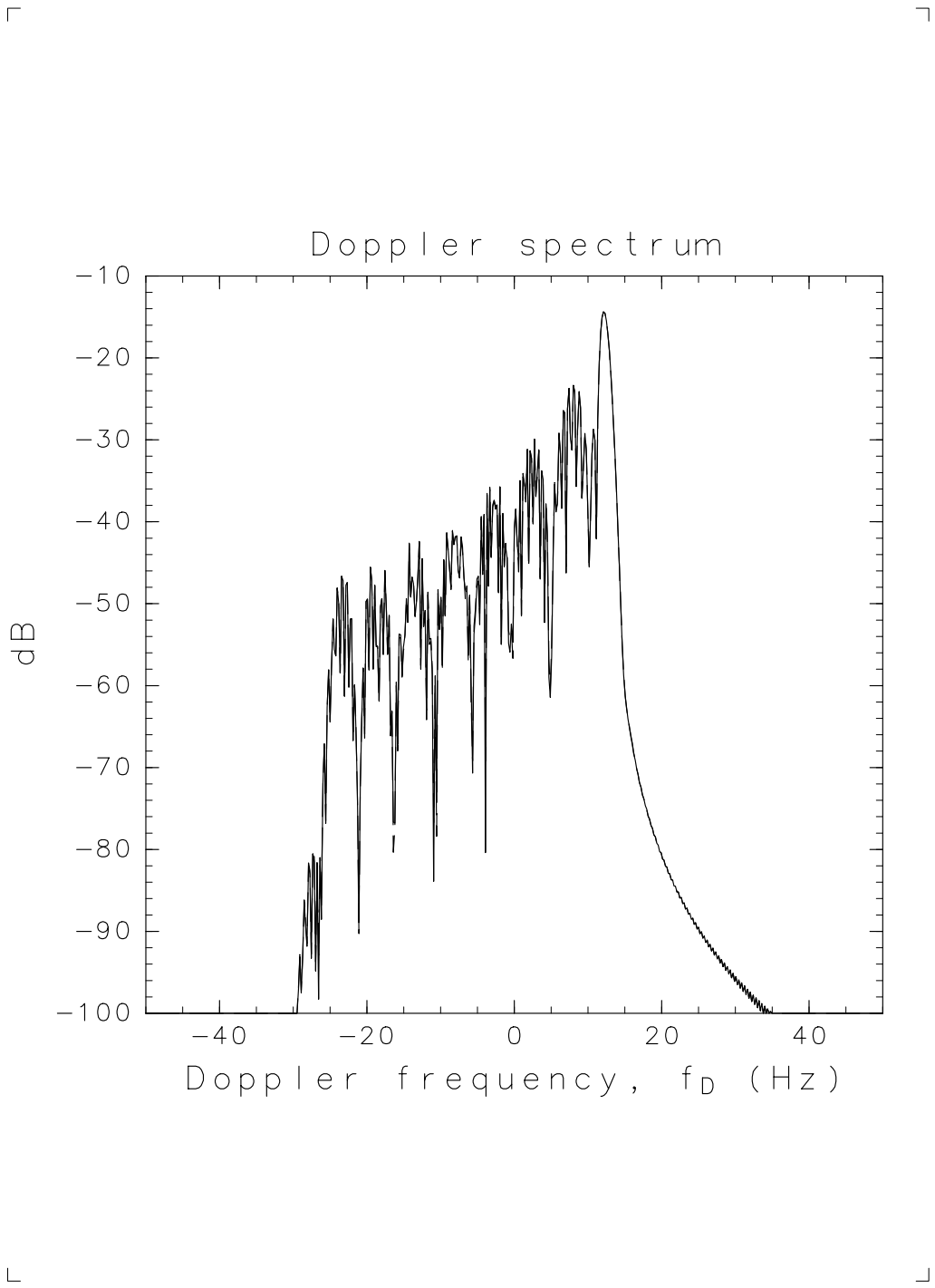
Figure 4: Comparison of Doppler spectra estimated from KA (solid line) and MFIE (dashed line). Note that the dashed line overlaps the solid line.
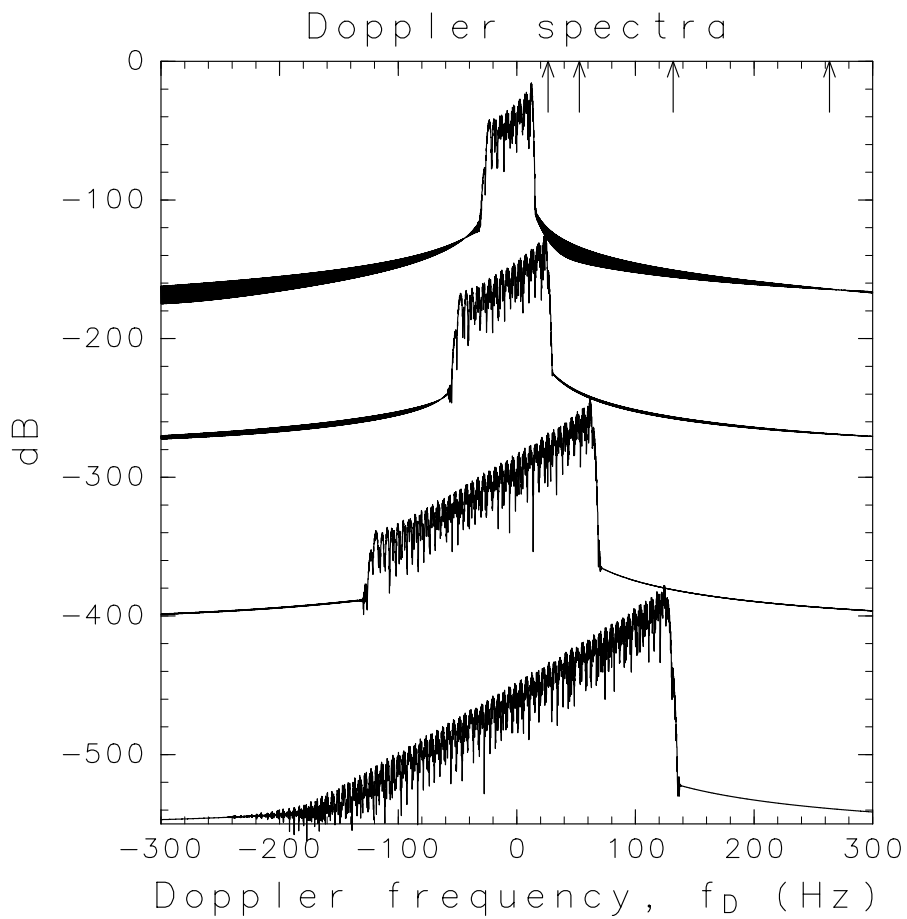
Figure 5: Doppler spectra for various radio frequencies estimated from KA. Radio frequencies are respectively $f_0 = 1, 2, 5$ and 10 GHz from top to bottom. Each Doppler spectrum is plotted by shifting 100 dB from the top. The arrows on the upper horizontal axis indicate the positions of the wave phase velocity-Doppler frequencies for each radio frequency.
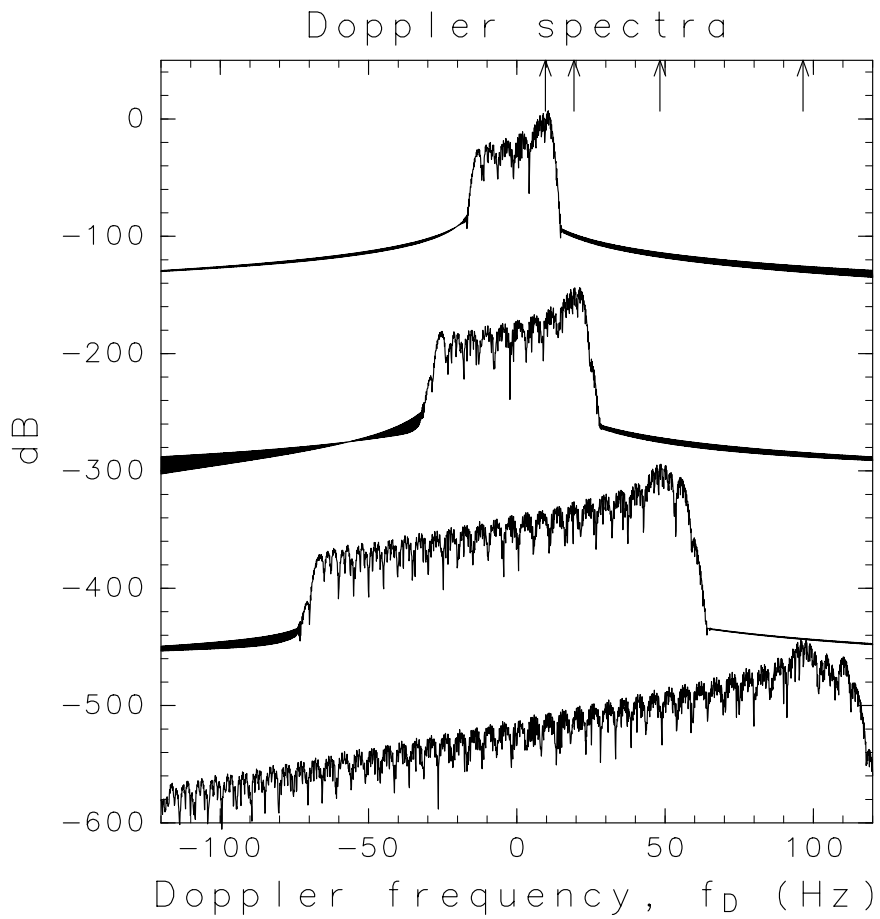
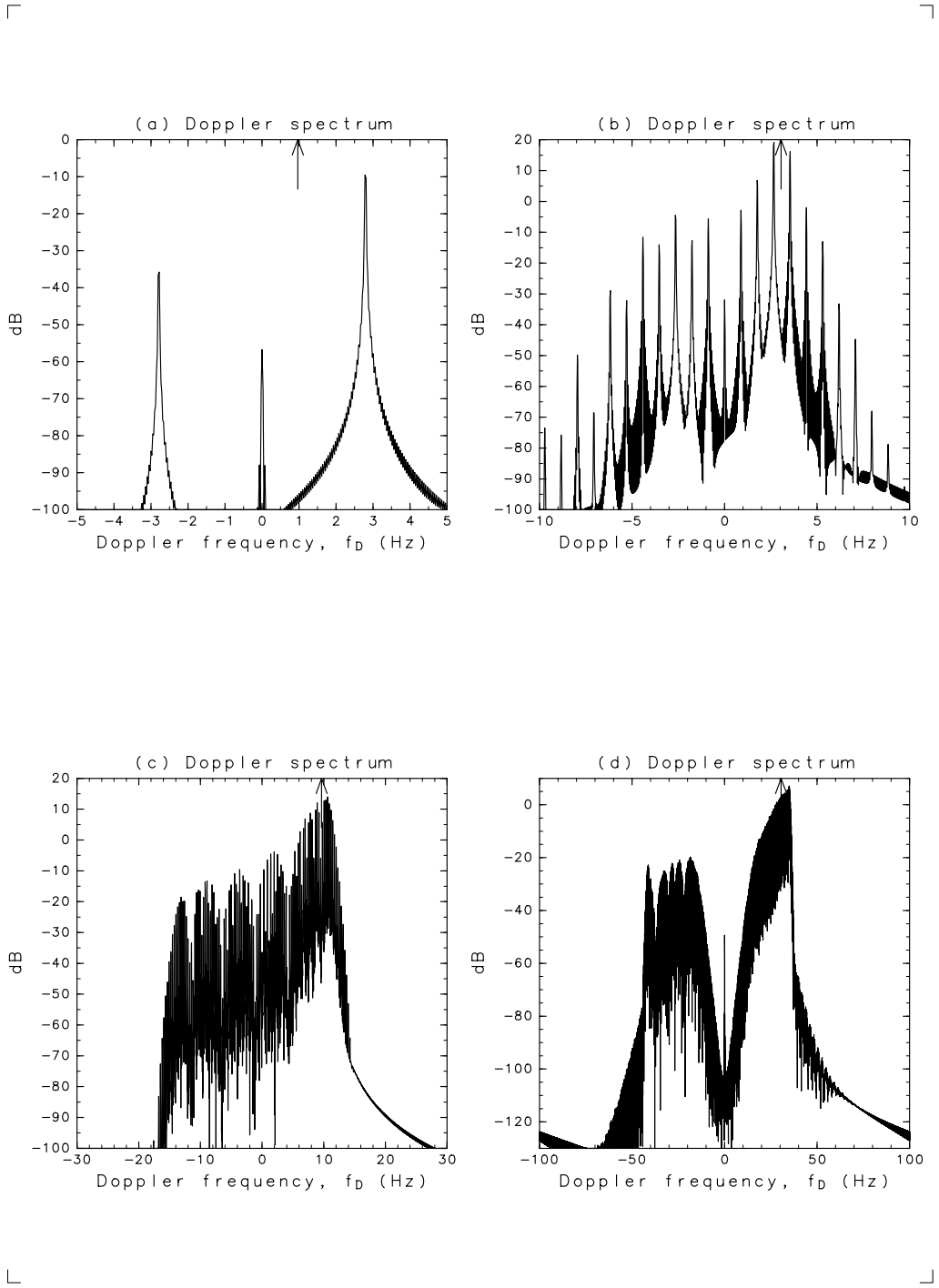Figure 6: Same as Figure 5 but $\theta_i = 15°$. Each Doppler spectrum is plotted by shifting 150 dB from the top.

Figure 7: Doppler spectra for various wave amplitude $A_{w0} = (1/20)\lambda_{w0}$ m and $\theta_i = 15°$ estimated from KA. The arrows on the upper horizontal axis indicate the positions of the wave phase velocity-Doppler frequencies for each wave amplitudes (wavelengths). (a) $A_{w0} = 0.01$ m, (b) $A_{w0} = 0.1$ m, (c) $A_{w0} = 1$ m, (d) $A_{w0} = 10$ m.
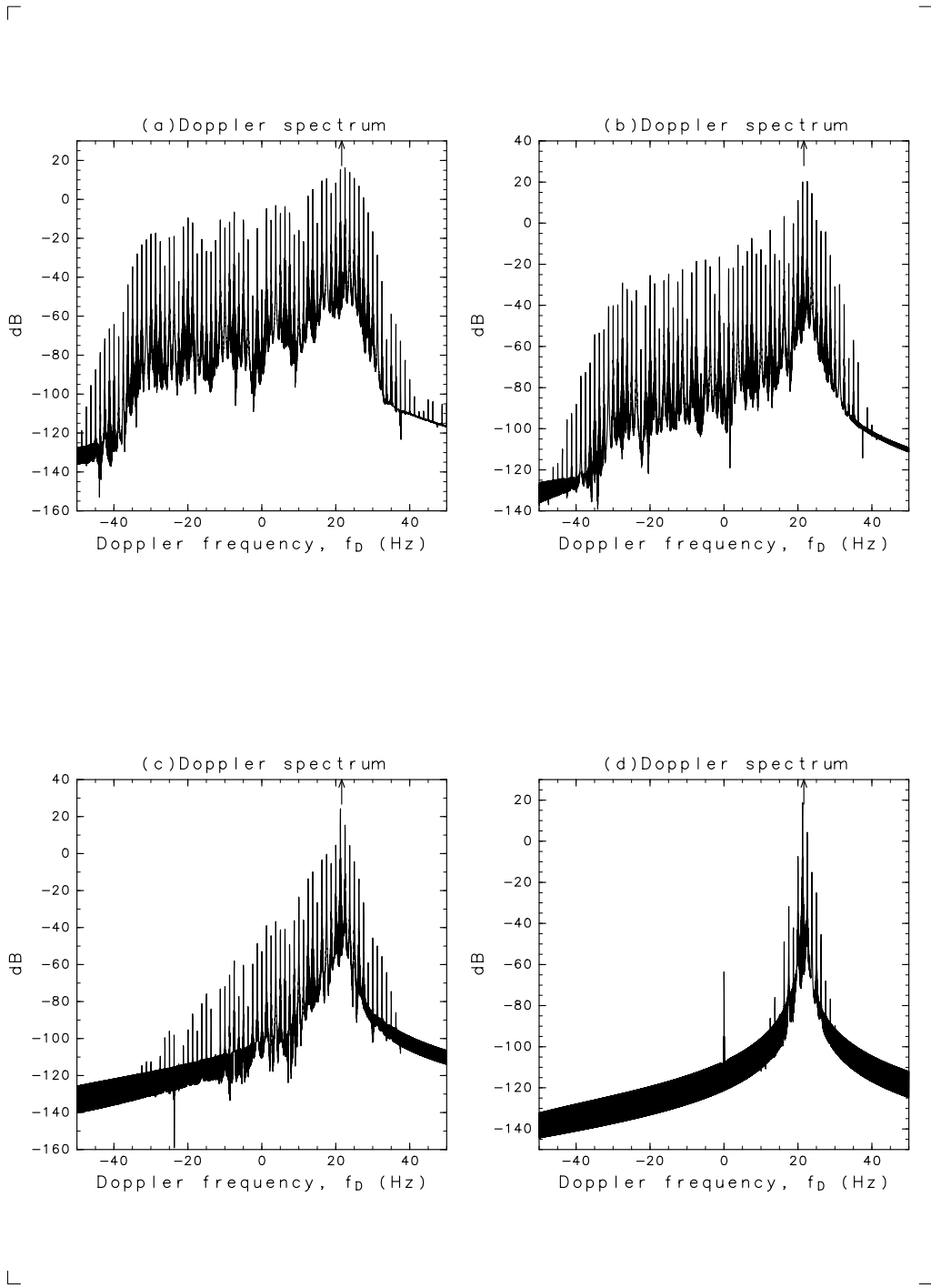
26

Figure 8: Doppler spectra for various effective lengths L_{eff} estimated from KA. The arrows on the upper horizontal axis indicate the positions of the wave phase velocity-Doppler frequencies for each radio frequency. (a) $L_{eff} = 0.1\,\mathrm{m}$, (b) $L_{eff} = 0.3\,\mathrm{m}$, (c) $L_{eff} = 1.0\,\mathrm{m}$, (d) $L_{eff} = 5.0\,\mathrm{m}$.

27